# Hybrid optimization of low-thrust many-revolution trajectories with coasting arcs and longitude targeting for propellant minimization

Jimenez-Lluva, David; Root, Bart

**DOI**
10.1016/j.actaastro.2020.06.015

**Publication date**
2020

**Document Version**
Final published version

**Published in**
Acta Astronautica

Acta Astronautica 177 (2020) 232–245

Contents lists available at ScienceDirect

Acta Astronautica

journal homepage: www.elsevier.com/locate/actaastro

# Hybrid optimization of low-thrust many-revolution trajectories with coasting arcs and longitude targeting for propellant minimization

David Jimenez-Lluva*, Bart Root

*Department of Astrodynamics and Space Missions, Delft University of Technology, Kluyverweg 1, 2629, HS Delft, the Netherlands*

ARTICLE INFO

*Keywords:*
Optimization
Low-thrust
Time-minimization
Propellant-minimization
Coasting arcs
Longitude-targeting

ABSTRACT

Despite the ongoing advancements in low-thrust propulsion technology and the rise of all-electric satellite platforms, low-thrust spacecraft trajectory optimization remains a complex field of research. Shape-based approximations are predominant in interplanetary applications, but they are generally unsuitable for many-revolution trajectories, common in terrestrial applications. Indirect optimization methods allow for global optimization of many-revolution trajectories, but their mathematical complexity generally requires significant simplifications of the dynamical model, and they must be re-derived for any modification to the system dynamics or constraints. Conversely, direct optimization methods exhibit larger convergence radii and are flexible for application in different problems yet suffer from impractical computational times due to large design vectors.

This paper presents a methodology for the optimization of low-thrust many-revolution trajectories, employing a hybrid combination of indirect and direct optimization methods. Similar hybrid approaches have been shown to be highly reliable for minimum-time trajectories. This methodology preserves similar performance while additionally enabling minimum-propellant optimization, through a mechanism that allows for coasting (non-thrusting) arcs, as well as targeting of the final geodetic-longitude. To reduce the propagation load of the methodology, we combine an orbital averaging scheme with a differential evolution algorithm, leading to a global optimization process with a practical computational effort. The analytical nature of the methodology reduces the number of optimization variables and its computational counterpart provides unmatchable flexibility for a configurable force and perturbation model as well as operational constraints fulfilment.

The approach is applied to an unperturbed and a $J_2$-perturbed GTO-GEO transfer, revealing a 0.03% and a 0.4% error, for time- and propellant-minimization respectively, relative to the reference optimal trajectories. This proves that the method can match the performance of former hybrid approaches while additionally allowing for engine on/off switching. Moreover, the inclusion of the $J_2$ perturbation shows that, in contrast to indirect methods, it can accommodate modifications to the system dynamics without the need to re-derive the optimal control laws. Furthermore, a superior convergence radius of the optimization problem is demonstrated for the hybrid method, with respect to a reference indirect method, through the simultaneous optimization for minimum-propellant expenditure and final geodetic-longitude targeting. This research constitutes a significant advancement for space mission design and satellite operations, because it simultaneously harnesses the advantages of indirect and direct methods with broader flexibility than the popular indirect approaches and enhanced functionality than the former hybrid methods published in literature.

## 1. Introduction

With the development of electric propulsion technology over the recent decades, the field of low-thrust trajectory optimization has regained a lot of interest. In interplanetary applications, the use of shape-based approximation methods is predominant [1,2]. Nonetheless, these generally perform worse in many-revolution trajectories [1,2], such as terrestrial orbital transfers, which is the focus of this study. In addition to shape-based approaches, there have been many other strategies developed to yield optimal and near optimal trajectories. These can generally be classified into direct methods [3,4] or indirect methods [5,6].

*Abbreviations:* CI, Continuous Integration; EOM, Equations of Motion; OA, Orbital Averaging; OCP, Optimal Control Problem; TPBVP, Two Point Boundary Value Problem; RSW, Radial local orbit frame

* Corresponding author.
*E-mail address:* davidjimenezlluva@gmail.com (D. Jimenez-Lluva).

https://doi.org/10.1016/j.actaastro.2020.06.015
Received 28 February 2019; Received in revised form 11 May 2020; Accepted 8 June 2020
Available online 27 June 2020

Indirect approaches require the analytical derivation of the Two-Point-Boundary-Value-Problem (TPBVP) through the optimality conditions of the Optimal Control Problem (OCP). This process employs a Hamiltonian equation that is set up from the objective function of the optimization and the known Equations of Motion (EOM). The optimal control laws can be found through the first and second derivatives of the Hamiltonian with respect to all control parameters, whereas the EOM of the optimal system co-states – also known as system adjoints – follow from the derivatives with respect to the state variables [7]. The main advantage of indirect methods is that they allow for reaching the global optimum due to the analytical formulation of the TPBVP. Additionally, this analytical derivation also results in significantly fewer optimization parameters than direct methods, leading to lower computational times [5,6]. Conversely, the underlying mathematical complexity limits the convergence radius of the optimization problem, such that even if a highly experienced user succeeds in analytically deriving the TPBVP of a very complex optimization problem, the resulting formulation might not converge to a feasible solution [8]. Consequently, orbital perturbations are partially neglected in indirect formulations, which limits the solution accuracy. Furthermore, the entire analytical formulation must be re-derived for any adjustment to the problem. This constitutes an important limitation for its practical applicability, e.g. in mission concept generation, because even a minor adjustment such as the inclusion of the $J_2$ perturbation requires a complete re-derivation of the TPBVP, which is a significantly labour-intensive task and requires a thorough experience of this field.

On the other hand, direct – or computational – approaches transcribe the OCP to a parameter optimization problem, employing nonlinear programming to iteratively solve for the control parameters that minimize an objective function while satisfying the equations of motion and boundary conditions. The main advantage of direct methods is the versatility of their computational nature, which allows for modifying the force model, constraints, and optimization objectives without the need to modify the formulation. Additionally, they often exhibit larger convergence radii than indirect methods, meaning that the resulting formulation is more likely to converge to a feasible solution than an indirect method for complex optimization problems [8]. This makes them an appealing asset for many-revolution low-thrust trajectories under sophisticated combinations of perturbing forces, operational constraints, or optimization objectives. However, due to the lack of the analytical optimal control derivation, direct methods often converge to local optima and, additionally, they yield exceptionally large design vectors (i.e. thousands of optimization variables) which lead to impractical computational times for complex problems. Therefore, direct methods are ideal for few-revolution trajectories, such as interplanetary transfer trajectories, rather than many-revolution trajectories [9].

Hybrid methodologies aim to harness the benefits of both direct and indirect approaches while avoiding their drawbacks. A benchmark [10] of the former hybrid formulations [11,12] demonstrated a 0.03% error with respect to the analytical global optimum computed with a reference indirect method [5] for a minimum-time GTO-GEO trajectory. The critical shortcoming of the former hybrid approaches published in literature is that they all assume a constant thrust throughout the trajectory, which results in ill-conditioning of propellant-minimization, as the results are severely similar to the minimum-time trajectories and too far from the analytical minimum-propellant solutions of indirect methods [11,12]. This constitutes a critical limitation because propellant minimization is of paramount importance for most applications, both in LEO and GEO. Although minimal transfer times are desirable in most cases, the ideal solution is generally a trade-off between minimizing the time-of-flight and the propellant expenditure. Additionally, the former hybrid approaches did not allow for targeting of the final geodetic-longitude, which is an essential ability for many applications, such as rendezvous missions or the positioning of GEO telecommunication satellites.

The primary objective of this research is to develop a methodology that allows for coasting (non-thrusting) arcs and thus demonstrate that the hybrid approach can match the solution accuracy of indirect methods for propellant-minimization, and to demonstrate that the optimal control laws do not need to be rederived for changes in the system dynamics. Furthermore, the secondary objective is to demonstrate its superior convergence performance to the indirect approach by optimizing for propellant-minimization while simultaneously targeting a desired geodetic longitude, which is not feasible for the reference indirect method [5], thus unlocking the full potential of the hybrid method.

## 2. Material and methods

This section describes the dynamical model employed and the underlying assumptions, followed by the description of the alternative propagation schemes implemented and the details on the optimization algorithm.

### 2.1. Dynamical model

The trajectory initial boundary conditions vector $\vec{\alpha}$ is expressed using the Keplerian orbital elements shown in Eq. (2.1), whereas the terminal conditions vector $\vec{\mathfrak{a}}$ employs the geodetic longitude $\Lambda$ instead of the true anomaly $\theta$:

$$\vec{\alpha} = [a_0, e_0, i_0, \Omega_0, \omega_0, \theta_0]^T \tag{2.1}$$

$$\vec{\mathfrak{a}} = [a_f, e_f, i_f, \Omega_f, \omega_f, \Lambda_f]^T, \tag{2.2}$$

where the index 0 indicates the conditions at $t = t_0$ and the index $f$ denotes the conditions at $t = t_f$; $t_f$ is hereafter used to denote the final time. The state vector $\vec{x}$ used in the propagation employs the set of modified equinoctial elements [13,14] to avoid the singularity of Keplerian elements, as well as the spacecraft mass $m$, see Eq. (2.3). The definition of the equinoctial elements with respect to the Keplerian elements can be found in Appendix A.

$$\vec{x} = [p, f, g, h, k, L, m]^T \tag{2.3}$$

The total disturbing acceleration vector acting on the spacecraft is shown in Eq. (2.4) and includes the thrust acceleration vector $\vec{a}_T$ and the perturbing acceleration, $\vec{a}_{J_2}$, caused by the oblateness of the Earth, or the $J_2$-effect. All other orbital perturbations are neglected as they were not employed in the reference indirect optimization study hereby used for validation [5].

$$\vec{a}_d = \vec{a}_T + \vec{a}_{J_2} \tag{2.4}$$

These individual accelerations experienced by the spacecraft are expressed in the RSW radial local orbit frame illustrated in Fig. 1. This frame is expressed mathematically in Eq. (2.5), where the vectors $\vec{r}$ and $\vec{v}$ constitute the Cartesian coordinates in the Earth centred fixed frame.

$$\boldsymbol{Q}_{RSW} = [\hat{q}_r \hat{q}_s \hat{q}_w] = \left[ \frac{\vec{r}}{\|\vec{r}\|} \frac{(\vec{r} \times \vec{v}) \times \vec{r}}{\|\vec{r} \times \vec{v}\| \|\vec{r}\|} \frac{\vec{r} \times \vec{v}}{\|\vec{r} \times \vec{v}\|} \right] \tag{2.5}$$

The $J_2$ acceleration vector expressed in the RSW frame using equinoctial elements is provided in Appendix A. The thrust acceleration vector $\vec{a}_T$ is defined in Eq. (2.6) in terms of the three control parameters to be optimized: the thrust yaw steering angle $\alpha$, the thrust pitch steering angle $\beta$, and the thrust magnitude $T$:

$$\vec{a}_T = \frac{T}{m} [\sin\alpha \cos\beta, \cos\alpha \cos\beta, \sin\beta]^T \tag{2.6}$$

Using the equinoctial formulation and the $\vec{a}_d$ vector in the $\boldsymbol{Q}_{RSW}$ frame, the system dynamics are provided by Gauss' form of the Lagrange planetary equations, which are shown in Eq. (2.7) in matrix form.

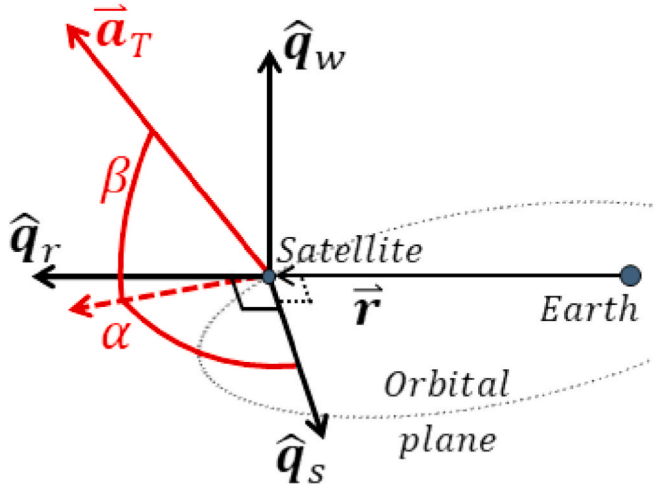


**Fig. 1.** Illustration of the RSW local orbit frame.

$$\frac{d\vec{x}}{dt} = \boldsymbol{A}\,\vec{a}_d + \vec{b} \tag{2.7}$$

The definition of the system dynamics matrix $\boldsymbol{A}(\vec{x})$ and the offset vector $\vec{b}$ are provided in Appendix A.

### 2.2. Propagation techniques

The two implemented alternative propagation schemes are: Continuous Integration (CI) and Orbital Averaging (OA). CI entails the classical propagation approach, where the state of the orbit is propagated from $t = t_0$ to $t = t_f$ using $n_p$ propagation steps per revolution. Conversely, OA aims to reduce the propagation effort through an averaged set of state derivatives to propagate over $n_{oa}$ steps in the order of days.

CI yields high-accuracy for all orbital elements, whereas OA sacrifices the accuracy of the rapidly changing element, i.e. true longitude, for computational speed. OA can be employed without a significant loss of accuracy for the other elements thanks to their smooth and gradual evolution in low-thrust trajectories. The error of the minimum-time LEO-GEO low-thrust transfer computed using OA steps of 5 days was shown to be 0.001% relative to the analytical solution [10]. Conversely, CI is the computationally more expensive alternative but allows for targeting the final geodetic longitude in the optimization, which is critical for GEO positioning or rendezvous applications.

The implemented logic for both schemes is very similar, as shown in Fig. 2. The inputs employed in the propagation are the initial orbit state $\vec{x}_0$ and the design vector $\vec{y}$ containing the optimization variables: the system co-states required for the optimal control law computation, and the transfer time needed for the stopping criteria. Further details about the design vector can be found in subsection 3.2. Upon each propagation step, the propagator evaluates whether any constraint is violated because some design-parameter combinations may lead to hyperbolic orbits, re-entry trajectories, or solutions that do not satisfy the operational constraints.

For both propagators, the chosen integration scheme is a fixed-step Runge Kutta 4 (RK4), yielding acceptable accuracy. Both OA and CI employ a state propagatation with $n_p$ steps per orbital revolution, using an equi-distant grid in true longitude instead of time to enhance the propagation accuracy near perigee. Since the system dynamics are expressed with respect to time, the true longitude propagation step $\Delta L = 2\pi/n_p$ must be converted to instantaneous time-steps at every epoch, $\Delta t = \Delta L(dL/dt) = (2\pi/n_p)(dL/dt)$, using the computed value of $dL/dt$ from Eq. (2.7). The difference is that CI iterates this process for every revolution of the trajectory until $t$ reaches $t_f$, whereas OA averages the $n_p$ computed state derivatives in the first revolution and uses $(d\vec{x}/dt)_{avg}$ to propagate through each of the $n_{oa}$ steps. At the start of each OA propagation step, $(d\vec{x}/dt)_{avg}$ is recalculated to account for the secular variations of the orbital elements. As shown in Eqs. (2.8) and (2.9), the averaged derivative is approximated through a trapezoidal scheme:

$$\left(\frac{d\vec{x}}{dt}\right)_{avg} = \frac{1}{P}\int_{t_0}^{t_0+T_{orb}} \frac{d\vec{x}}{dt}\,dt \tag{2.8}$$

$$\left(\frac{d\vec{x}}{dt}\right)_{avg} \approx \frac{1}{P}\sum_{i=0}^{n_p-1} \frac{\left[\frac{d\vec{x}}{dt}\Delta t\right]_{t=t_i} + \left[\frac{d\vec{x}}{dt}\Delta t\right]_{t=t_{i+1}}}{2}, \tag{2.9}$$

where $P$is the instantaneous orbital period. Because the varying step-size is a function of the equidistant true longitude step-grid, the accuracy of the rapidly-changing element, $L$, is lost in the process. Since the short-period variations of the slowly-changing elements are generally not of interest, OA is a great asset for most low-thrust optimizations. Nonetheless, CI may be used in special cases requiring the targeting of the final geodetic longitude.

### 2.3. Differential evolution algorithm

For the optimization algorithm, the Differential Evolution (DE) algorithm [15] was selected due to its simplicity, yet any other algorithm from the metaheuristic family is deemed suitable due to their ability to converge to the global optima. This choice is ideal for this study, despite the characteristically long optimization times of DE algorithms, because the computational time of the optimization is not a primary requirement to demonstrate the potential of the hybrid method.

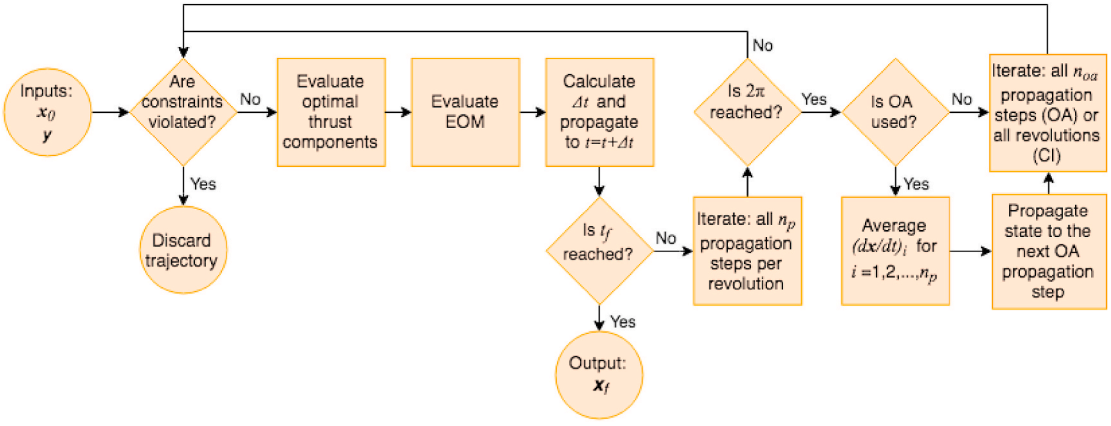


**Fig. 2.** Work-flow logic of the propagation scheme.

The DE optimizer employed is an implementation of the original DE algorithm [15], written in Fortran90 and freely available in Ref. [16]. It is the simplest variation among DE algorithms and its stopping criteria rely solely on a bounded number of iterations. The maximum number of iterations is set to 1000 and the DE optimizer parameters are set exactly as in the indirect optimization study hereby used for validation [5]: the cross-over rate and the mutation scale factor are set to 0.8 and 0.6 respectively, and the population size is taken to be ten times the number of optimization variables (i.e. 110 and 130 for the time- and propellant-minimization problems respectively, see subsection 3.2). Lastly, all DE optimizations provided in this paper are evaluated using an Intel Core i5-4590 CPU with 3300 MHz and 8.00 GB RAM.

## 3. Theory

The hybrid methodology employs the necessary first-order optimality conditions of the Optimal Control Problem (OCP) without fully deriving the Two-Point-Boundary-Value-Problem (TPBVP). Instead of deriving the optimal equations of the system co-states to complete TPBVP like indirect methods, it linearizes the EOM for the system co-states and solves the OCP in a direct approach. This method is more efficient than direct approaches because its derivation of the necessary optimality conditions leads to significantly fewer optimization variables and thus practical computational times. Additionally, it is superior to indirect methods because it retains the flexibility of direct approaches. This allows the user to modify the problem - i.e. adjust the force model, operational constraints, or optimization objectives - with minor effort because there is no need to analytically re-derive the TPBVP like in indirect methods.

Theoretically, a hybrid formulation should be less accurate than an indirect derivation, because the linearized co-state EOM may not satisfy their analytically optimal EOM. However, previous studies on low-thrust Earth-based transfers using the hybrid formulation with such simplified co-state dynamics [11,12] showed high accuracy for minimum-time trajectories, with a demonstrated 0.03% error relative to the reference GTO-GEO optimal trajectory.

### 3.1. Optimal control problem

An OCP entails a system with a state vector and control input defined by $\vec{x}(t)$ and $\vec{u}(t)$, respectively, and whose system dynamics are described by the set of ordinary differential equations in Eq. (3.2):

$$\vec{u}(t) = [\alpha(t),\beta(t),T(t)]^T \tag{3.1}$$

$$\frac{d}{dt}\vec{x}(t) = f(\vec{x}(t),\ \vec{u}(t),\ t), \tag{3.2}$$

where the thrust magnitude and steering angles can be a function of time.

The standard form of the objective function of an OCP is shown in Eq. (3.3), the function used in this methodology is described in depth in subsection 3.3. According to Pontryagin's Minimum Principle [7], the optimal conditions leading to the global minimum are those that minimize the Hamiltonian equation, shown in standard form in Eq. (3.4).

$$F = \Phi(\vec{x}(t_f),\ t_f) + \int_{t_0}^{t_f} \mathscr{L}(\vec{x}(t),\ \vec{u}(t),\ t)dt \tag{3.3}$$

$$\mathscr{H} = \mathscr{L} + \vec{\lambda}^T \cdot \frac{d\vec{x}}{dt}, \tag{3.4}$$

where $\Phi$ and $\mathscr{L}$ are known as the Mayer and Lagrange functions. The system co-states vector $\vec{\lambda}$, also referred to as the system adjoints vector, indicates the relative priority of the variations of the state parameters over time. The co-state vector for the problem at hand and the resulting Hamiltonian are shown in Eqs. (3.5) and (3.6):

$$\vec{\lambda} = [\lambda_p,\lambda_f,\lambda_g,\lambda_h,\lambda_k,\lambda_m]^T \tag{3.5}$$

$$\mathscr{H} = \lambda_p\frac{dp}{dt} + \lambda_f\frac{df}{dt} + \lambda_g\frac{dg}{dt} + \lambda_h\frac{dh}{dt} + \lambda_k\frac{dk}{dt} + \lambda_m\frac{dm}{dt} \tag{3.6}$$

The Karush-Kuhn-Tucher first-order necessary condition for optimality states that the first derivative of the Hamiltonian with respect to the control variables – $\alpha$, $\beta$, and $T$– must be null at a singular point [7], see Eq. (3.7). Additionally, the Legendre-Clebsch condition, states that the second derivative must be positive for a minimum solution [7], see Eq. (3.8).

$$\frac{\partial\mathscr{H}}{\partial\vec{u}} = \vec{0} \tag{3.7}$$

$$\frac{\partial^2\mathscr{H}}{\partial\vec{u}^2} > \vec{0} \tag{3.8}$$

The application of Eqs. (3.7) and (3.8) lead to the optimal control laws $\vec{u}^* = [\alpha^*,\beta^*,T^*]^T$, derived in Appendix B, which are only a function of the system state and co-states $\vec{u}^*(t) = f\left(\vec{x},\ \vec{\lambda},\ t\right)$, see Eqs. B7-B.8, B.19-B.20, and B.22-B.23. These can be substituted in Eq. (2.7), yielding $d\vec{x}(t)/dt = f\left(\vec{x}(t),\ \vec{\lambda}(t),\ t\right)$.

Albeit necessary, the conditions in Eqs. (3.7) and (3.8) are not sufficient for optimality [7] and one must derive the following condition for every system co-state in the TPBVP:

$$\frac{d\vec{\lambda}}{dt} = -\frac{\partial\mathscr{H}}{\partial\vec{x}} \tag{3.9}$$

In indirect approaches, it is the derivation of Eq. (3.9) which leads to the EOM of the optimal co-states [5,6], $d\vec{\lambda}(t)/dt = f\left(\vec{\lambda}_0,\ \vec{x}(t),\ t\right)$, and only their initial values $\vec{\lambda}_0$ remain to be optimized, such as the case of the reference indirect approach [5]. However, the derivation of Eq. (3.9) is circumvented in the hybrid methodology through a linearization of the system co-states, because applying this condition would significantly limit the applicability of the methodology, see subsection 3.2.

### 3.2. Linearization of the Co-State equations of motion

A change to the dynamic model $\vec{x}(t)$ does not affect the optimality conditions in Eqs. (3.7) and (3.8), because these entail only the partial derivation of the Hamiltonian with respect to the controls $\vec{u}(t)$. However, it does affect the partial derivation of $\mathscr{H}$ with respect to $\vec{x}(t)$(Eq. (3.9)) and this is a limitation of indirect methods because any adjustment to the state EOM requires rederiving this condition. For example, the reference indirect approach [5] disregards all orbital perturbations in the dynamic model, and the inclusion of the $J_2$ perturbation requires a complete re-derivation of the optimal co-state EOM (Eq. (3.9)).

The hybrid methodology circumvents the need to derive the analytical co-state EOM (Eq. (3.9)) by employing a linearized set of co-state EOM, which enables the application to a wide range of problems with different dynamical models. This is achieved by dividing the trajectory into segments, optimizing the co-state values at the boundaries of each segment, and using linear interpolation in-between.

Although a greater number of segments should better approximate the optimal co-state EOM in theory, it is observed that using more than one segment yields only small accuracy enhancements that are not worth the increased computational load. Hence, the methodology hereby presented corresponds to a co-state linearization using only the boundary values of the co-states, at $t = t_0$ and $t = t_f$:

$$\lambda_j(t) = (\lambda_j)_{t=t_0} + \frac{t-t_0}{t_f-t_0}(\lambda_j)_{t=t_f}, \tag{3.10}$$

**Table 1**
Values of the initial GTO(7°), target GEO, and error tolerances used in all optimization cases.

| | $a$[km] | $e$[deg] | $i$[deg] | $\omega$[deg] | $\Omega$[deg] | $\theta$[deg] | $\Lambda$[deg] |
|---|---|---|---|---|---|---|---|
| Initial GTO(7°) | 24505.9 | 0.725 | 7.0 | 0.1E-12 | 0.1E-12 | 0.1E-12 | n.a. |
| Target GEO | 42165.0 | 0.1E-12 | 0.1E-12 | n.a. | n.a. | n.a. | n.a. (28.5°E for case 3) |
| Maximum allowed final orbit error | 100.00 | 0.01 | 0.1 | 1.0 | 1.00 | n.a. | 1.00 |

where $j = 1,2, \ldots,6$ corresponds to indices of the components of the co-states vector $\vec{\lambda}$. The resulting design vector, i.e. the variables to be optimized, is shown in Eq. (3.11) and includes the 12 boundary values of the 6 co-state parameters, as well as the transfer time expressed in days:

$$\vec{y} = \left[ t_f, \vec{\lambda}_0^T, \vec{\lambda}_f^T \right]^T \tag{3.11}$$

The transfer time it is needed to perform the propagation to $t = t_f$, where the objective function is to be evaluated. Nonetheless, it should be clarified that the formulation remains a free-time problem and $t_f$ may still be minimized through the optimization objective function.

These 13 design parameters reduce to 11 for time-minimization purposes, because the minimum-time formulation employs continuous thrust, meaning that the control parameters reduce to $\vec{u}(t) = [\alpha(t),\beta(t)]^T$. Since the mass state parameter does not depend on the control variables, the mass co-state can be omitted in the Hamiltonian, see Eq. (3.6). This adjustment is very easy to implement because the massless Hamiltonian leads to the same optimal control laws as derived in Appendix B. This linearization of the system co-states avoids the problem dependency that arises from Eq. (3.9) and allows for a flexible and generic optimization method, because the optimal control laws that follow from the conditions in Eqs. (3.7) and (3.8) remain applicable despite adjustments to the problem.

### 3.3. Optimization objective function

The objective function employed (Eq. (3.12)) combines a multi-objective strategy with respect to time- and propellant-minimization, as well as targeting of the desired final orbit:

$$F = W_t t_f + W_m \left(1 - \frac{m_f}{m_0}\right) + \sum_{\{j=1\}}^{6} W_j (\varepsilon_j)^2, \tag{3.12}$$

where $W_t$ and $W_m$ are the optimization weights corresponding to the transfer time and mass expenditure, and $m_0$ and $m_f$ represent the initial and final satellite mass. $\varepsilon_j$ represents the scaled terminal orbit error for each of the $j = 1,2, \ldots,6$ Keplerian elements in $\vec{\text{æ}}$, and $W_j$ is the corresponding optimization weight. Although equinoctial elements are employed in the propagation, the objective function uses Keplerian elements such that the user can more intuitively tailor the desired target orbit. The scaling procedure implemented to compute $\varepsilon_j$ is defined in Eqs. (3.13)-(3.16):

$$e_j = |(æ_j)_t - (æ_j)_f| \tag{3.13}$$

$$c_j = \frac{1}{(e_j)_{UB} - (e_j)_{LB}} \tag{3.14}$$

$$r_j = 1 - (e_j)_{UB} c_j \tag{3.15}$$

$$\varepsilon_j = e_j c_j + r_j, \tag{3.16}$$

where $c$ and $r$ are auxiliary variables and $\vec{e}_{UB}$ and $\vec{e}_{LB}$ are the upper and lower bounds of the scaled final orbit error.

This scaling procedure is implemented to ensure that the optimizer will focus in minimizing the transfer time or the propellant expenditure only after the final orbit error satisfies the desired user-specified tolerances. The scaled final orbit errors $\varepsilon_j$ attain a value if it is $e_j$ is within the specified tolerances, $e_{LB} < e < e_{UB}$, and a value $\in (1, \infty)$ otherwise. Thus, the contribution of $(\varepsilon_j)^2$ in Eq. (3.12) becomes less important if $e_j \in (0,1]$, causing the optimization to focus on minimizing the first two terms in Eq. (3.12); yet it becomes increasing relevant for $e_j \in (1, \infty)$, and the optimizer therefore prioritizes the accurate targeting of the final orbit.

Additionally, this scaling procedure enhances automation and reduces the user fine-tuning effort in all applications. This is because the values of the scaled errors in $\vec{\varepsilon}$ all vary in similar orders of magnitude, such that the weights $W_j$ in Eq. (3.12) to be unity in nominal operations.

## 4. Results

The potential of the improved hybrid methodology is demonstrated through the optimization of a GTO-GEO trajectory for three different cases:

1. Time-minimization,
2. Propellant-minimization,
3. Propellant-minimization with simultaneous final geodetic longitude targeting.

This trajectory is chosen to enable the comparison with the reference analytical global optima [5] computed through an indirect method. The initial GTO, target GEO, and maximum allowed deviation employed in all cases are shown in Table 1. The term GTO(7°) is used hereafter used to indicate the orbital inclination, which may differ from other GTO.

The lower bounds $\vec{e}_{LB}$ of the final orbit errors are set to zero, i.e. an ideal transfer, and the upper bounds $\vec{e}_{UB}$ are set to the tolerances shown in Table 1. The satellite platform parameters used are: $m_0 = 2000.0$ kg, $T = 350.0$ mN, and $I_{sp} = 2000.0$s.

### 4.1. Minimum-time GTO(7°)-GEO trajectory

The following optimization case was covered as benchmark [10] on former hybrid methodologies [11,12], which employed a constant thrust assumption. The results are revisited here to facilitate the comparison with the minimum-propellant optimization, and are extended to evaluate the OA propagation, which was not employed in the benchmark [10].

The transfer is optimized with CI propagation for the unperturbed and $J_2$-perturbed scenarios, and the computed optimal thrust profile is then propagated with OA. This transfer targets only the first three Keplerian elements due to the singularities in $\Omega$ and $\omega$ in GEO; i.e. $W_a = W_e = W_i = 1.0$ and $W_\Omega = W_\omega = 0.0$. Furthermore, the transfer time weight is set to $W_t = 0.1$, the satellite's final angular position is a free variable, , and propellant-minimization is disregarded, $W_m = 0$.

Fig. 3 illustrates the 3D projections of the computed optimal $J_2$-perturbed trajectory, using a colour scale to indicate the evolution over time. The secular drift of the perigee is caused by the $J_2$ effect, and the colour overlap that occurs near apogee due to non-zero inclinations indicates that the apogee altitude is increased to enhance the inclination correction and decreased afterwards.

Table 2 shows the computed time of flight and propellant expenditure of the optimal trajectories for the unperturbed and $J_2$-perturbed transfers [10], relative to the analytical global optima computed with the reference indirect method [5]. It is worth mentioning that

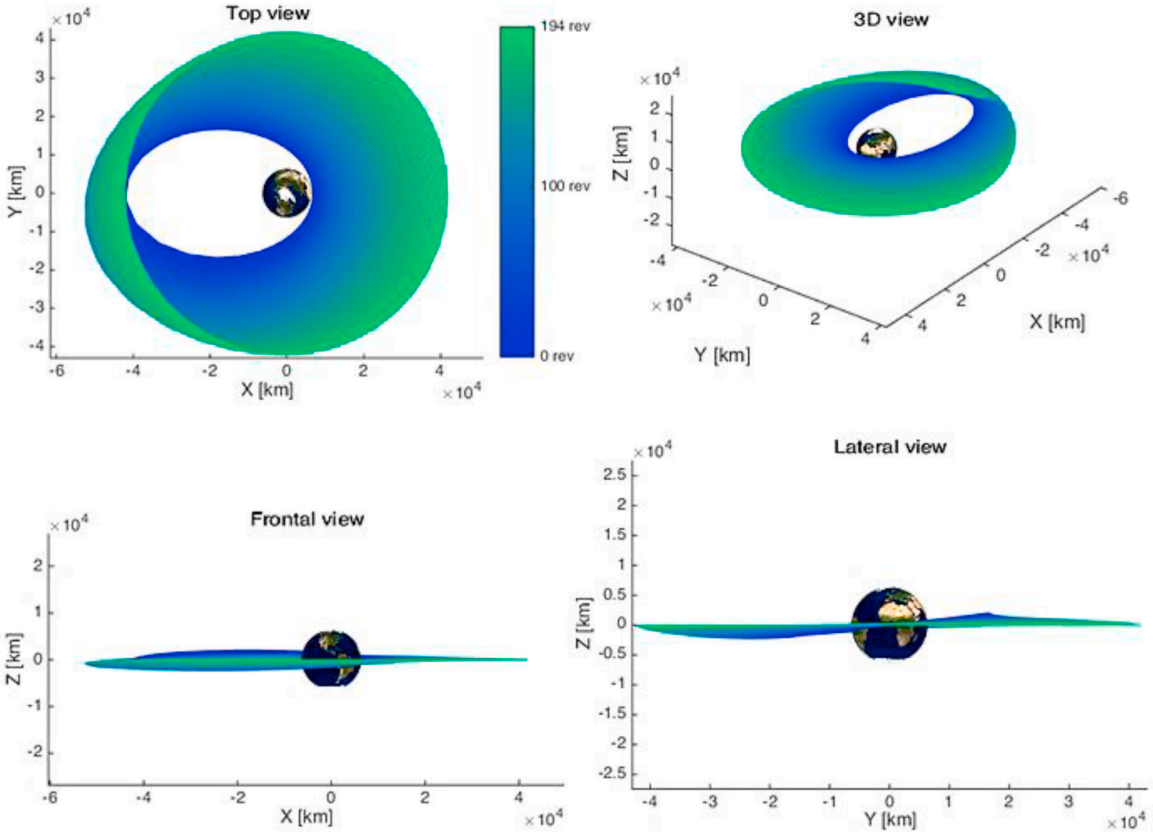


**Fig. 3.** Illustration of the computed optimal minimum-time GTO(7°)-GEO $J_2$-perturbed trajectory in top, 3D, frontal, and lateral views [10].

**Table 2**
Results for the unperturbed and $J_2$-perturbed GTO(7°)-GEO min-$t_f$ optimization [10].

| | $t_f$ [days] | $m_p$ [kg] |
|---|---|---|
| Calculated, unperturbed | 137.45 | 211.91 |
| Reference, unperturbed [5] | 137.41 | 211.86 |
| Calculated, $J_2$-perturbed | 137.71 | 212.32 |
| Reference, $J_2$-perturbed | 137.75 | 212.39 |

whereas the hybrid method readily allows for adding the $J_2$ effect in the optimization, the reference indirect approach must be analytically re-derived for such adjustments. Hence, the reference analytical optimal solutions correspond to two different analytical derivations based on the reference indirect method [5].

The computed optimal trajectories show a significant resemblance with the reference analytical global optima with a percentage error of 0.03% for both cases. The inclusion of the $J_2$ effect increases the transfer time by 2 h and the computational effort by about 5%, with a total optimization time of 118 and 124 min respectively for the two cases.

Table 3 shows that the deviation of the final achieved orbits from the desired GEO is very low despite the relatively broad tolerances employed in $\vec{e}_{UB}$. Additionally, the unperturbed optimal thrust profile was propagated with OA, yielding an error relative to CI of 0.00 kg for $m_f$, which is to be expected because the mass flux varies linearly with time; and an error of 35.66 km, 0.012, and 0.008 deg for $a_f$, $e_f$, and $i_f$ respectively, which satisfies the tolerances from Table 1.

**Table 3**
Final achieved orbit for the optimal computed unperturbed and $J_2$-perturbed minimum-time transfers.

| | $a_f$ [km] | $e_f$ [−] | $i_f$ [deg] | $m_f$ [kg] |
|---|---|---|---|---|
| Unperturbed | 42164.65 | 5.53E-4 | 7.41E-5 | 1787.68 |
| $J_2$-perturbed | 42164.68 | 5.28E-4 | 2.59E-4 | 1788.09 |
| Target GEO | 42165.0 | 0.1E-12 | 0.1E-12 | n.a. |

### 4.2. Minimum-propellant GTO(7°)-GEO trajectory

The following case demonstrates the potential of the hybrid methodology for propellant-minimization. The trajectory is optimized using OA to reduce the computational time, neglecting the $J_2$ and all other perturbations as in the reference study [5]. The transfer time is fixed at certain values – $t_f$ = 150, 175, 200, 225, 250and 300 days – to enhance the convergence rate of the Differential Evolution (DE) optimizer. Because the stopping criteria of the simple DE algorithm employed relies solely on a bounded number of iterations, three DE executions are evaluated for each case to ensure convergence to global optima.

The 2D projections on the equatorial plane of the propellant-optimal 150-, 200-, and 250-day trajectories are shown in Fig. 4, together with the unperturbed 137-day time-optimal trajectory from the previous case. The coasting regions, depicted in grey, exhibit an expected pattern, with the engine switched off near perigee as the initial apogee radius is already close to the target value.

Fig. 5 portrays the computed optimal solutions, which closely approximate a reference analytical Pareto front [5]. This diagram shows the optimal $m_p$–$t_f$ combinations that are very useful for decision-making in mission design. The high accuracy of the computed optima demonstrates that the linearization of the co-state EOM does not significantly influence the resulting trajectories, even for the complex case of propellant-minimization. Thus, the hybrid method does not jeopardize the solution accuracy compared to the analytical global optima of the reference indirect method [5]. The random nature of the DE optimizer is also visible in Fig. 5, as some executions yield a mass expenditure exceeding 220 kg that is not visible in the graph. This signifies the need of executing multiple repetitions and reveals room for improvement in the

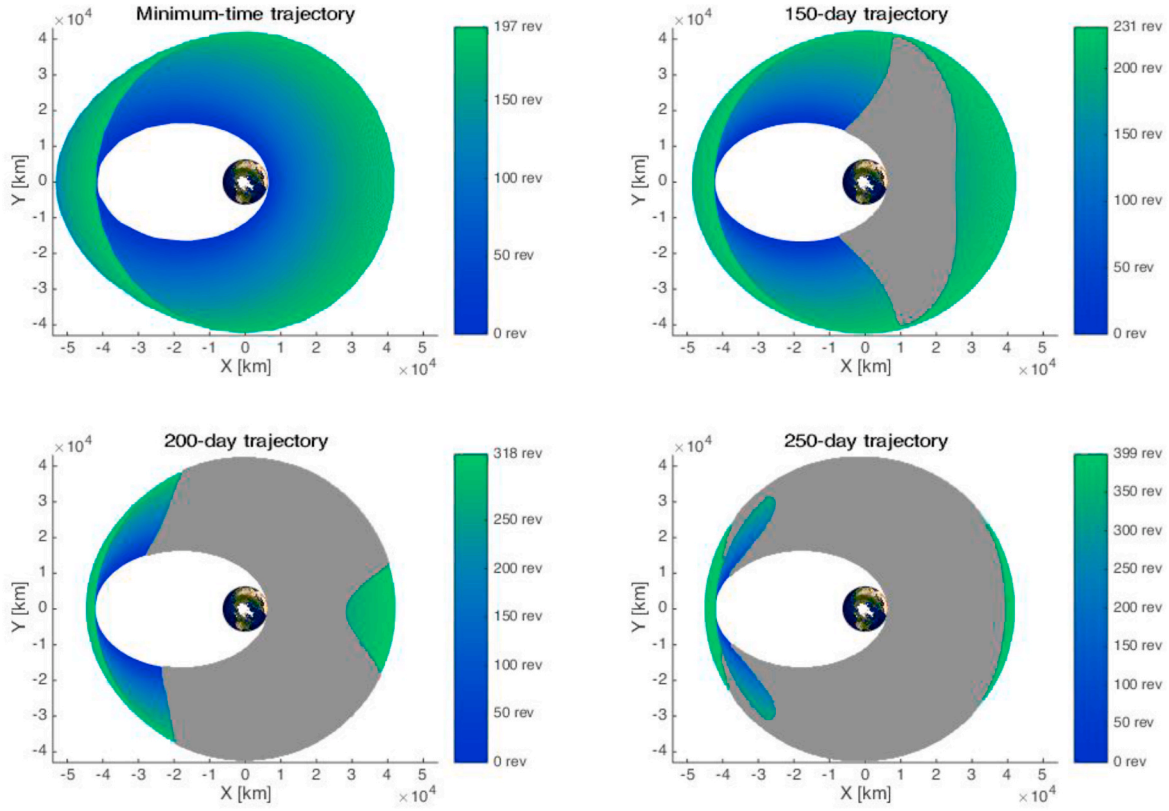


**Figs. 4.** 2D equatorial projections of the computed optimal minimum-propellant GTO(7°)-GEO unperturbed trajectory and coasting arcs (depicted in grey) for transfer times of 137 (minimum-time), 150, 200, and 250 days.

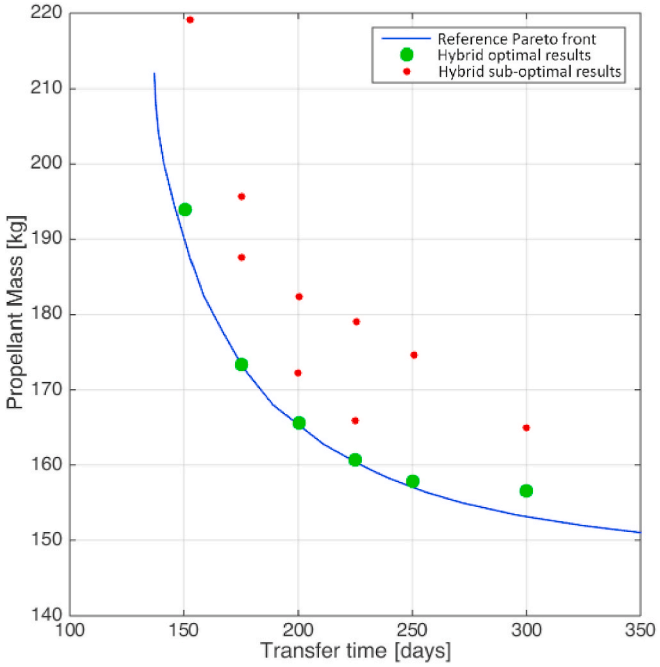


**Fig. 5.** Optimal $m_p$–$t_f$ computed solutions for the GTO(7°)-GEO unperturbed trajectory, compared to the reference analytical global optima [5].

DE algorithm used.

Table 4 presents the OA optimization results for the optimal 250-day optimal trajectory, as well as the CI simulation of the optimized parameters. As expected from the time-minimization case, the OA-CI error satisfies the tolerances from Table 1. It also reveals a 1 kg error in the propellant consumption, caused by the averaging of the coasting arcs, which is deemed acceptable yet indicates room for improvement in the averaging implementation. Unlike the time-optimal solutions, the final achieved orbit of the CI simulation deviates from the target GEO, with a percentage error up to 0.4% ($e_a$ = 153 km, $e_e$ = 0.002and $e_i$= 0.003deg). The mean computational time per DE execution was 30, 43, and 62 min for the 150-, 200-, 250-day trajectories respectively, which is considerably faster than the previous 118 min optimization thanks to OA propagation.

**Table 4**
Results for the 250-day minimum-propellant GTO(7°)-GEO optimization.

| | $a_f$ [km] | $e_f$ [−] | $i_f$ [deg] | $m_f$ [kg] |
|---|---|---|---|---|
| OA optimization result | 41986.91 | 1.26E-2 | 4.08E-2 | 1843.15 |
| CI propagation | 42011.98 | 2.29E-3 | 3.45E-2 | 1842.19 |
| OA-CI error | 25.07 | 1.03E-2 | 6.27E-3 | 0.96 |
| Target GEO | 42165.0 | 0.1E-12 | 0.1E-12 | n.a. |

### 4.3. Minimum-propellant GTO(7°)-GEO trajectory with longitude-targeting

This case demonstrates the superior convergence radius of the hybrid method relative to the reference indirect approach [5]. The GTO (7°)-GEO transfer is optimized for propellant-minimization while targeting the final geodetic longitude of 28.5°E. The transfer trajectory is propagated using CI with the transfer-time fixed at certain values ($t_f$ = 150, 175, 200, 250 and 300 days) to reduce the computational load. The $J_2$ perturbation is incorporated for a more realistic longitude targeting, and three DE repetitions are executed for each case.

Fig. 6 provides the computed optimal solutions as well as Pareto front the reference indirect study [5], which remains the closest reference data even though it does not incorporate the $J_2$ effect nor does it allow for longitude targeting. Unlike in the previous case, the computed optimal

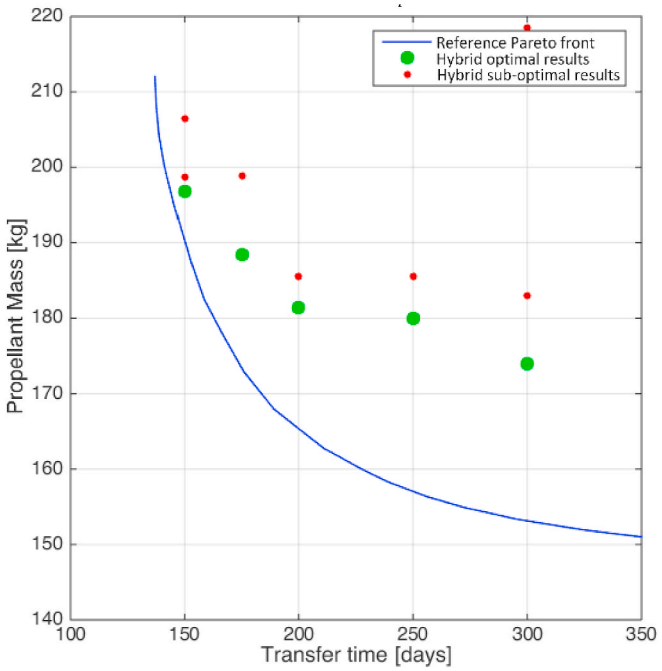


**Fig. 6.** Optimal $m_p$–$t_f$ computed solutions for the GTO(7°)-GEO(28.5°E) $J_2$-perturbed trajectory, compared to the reference analytical global optima for the unperturbed free-longitude trajectory [5].

solutions deviate slightly from the expected shape of a Pareto front and some of the sub-optimal solutions exceed the $m_p$ range of the figure.

An example of the final achieved orbit is shown in Table 5 for the 250-day transfer. It is observed that the deviation from the target orbit is larger than the previous cases and remains in the order of magnitude of the desired tolerances from Table 1.

Fig. 7 provides the illustrations of the 2D equatorial projections of the 150-, 175-, and 200-day propellant-optimal trajectories, together with the time-optimal $J_2$-perturbed 137-day trajectory from case 1. As expected, the coasting regions exhibit patterns concentrated near apogee and, unlike the previous case, they exhibit a non-symmetrical shape. This irregularity of the coasting regions is probably caused by the $J_2$ effect because the grey regions in Fig. 7 warped in the same direction as the clockwise drift of the apogee in the minimum-time transfer.

## 5. Discussion

The accurate results for time-minimization with and without the $J_2$ perturbation show that the optimal control laws of the hybrid method remain applicable despite modifications to the dynamical model. This is a major advantage over indirect methods because it guarantees the ability to modify the problem without jeopardizing its accuracy and, more importantly, without the need to analytically re-derive the two-point-boundary-value-problem. This makes the hybrid method a great asset for applications that aim to evaluate different combinations of dynamical models and constraint-sets in alternative mission designs.

The error with respect to the reference globally-optimal GTO-GEO trajectories [5] was, on average, 0.03% for the minimum-time solutions and 0.4% for the propellant-optimal GTO-GEO trajectories. This impressive evidence shows that, despite its simplified co-state dynamics, the hybrid method can reach the accuracy of the analytical global optima from the reference indirect method. The linearization of the system co-states, using only their boundary values, does not jeopardize the precise global optimization. Furthermore, it makes the hybrid method superior to direct approaches because it yields few optimization variables (11 or 13 for time- and propellant-minimization respectively) and thereby practical computational times. Nonetheless, this demonstration for the GTO-GEO transfer does not immediately imply that the method will yield such impressive performance in other complex problems. Therefore, more trajectories should be analysed in future research.

**Table 5**
Results for the 250-day $J_2$-perturbed minimum-propellant GTO(7°)-GEO (28.5°E) optimization.

| | $a_f$ [km] | $e_f$ [−] | $i_f$ [deg] | $m_f$ [kg] | $\Lambda_f$ [deg] |
|---|---|---|---|---|---|
| CI result | 42190.94 | 3.392E-4 | 1.404E-1 | 1819.73 | 28.48 |
| Target GEO | 42165.0 | 0.1E-12 | 0.1E-12 | n.a. | 28.50 |

Although the results for the simultaneous propellant-minimization and final geodetic longitude targeting are less robust and indicate room for improvement, the fact that the hybrid methodology yields feasible trajectories is evidence of a superior convergence radius than indirect approaches. This is because the reference indirect approach [5], which was analytically re-derived by a third party to include the $J_2$ effect and allow for longitude targeting does not converge to a feasible GTO-GEO trajectory for the desired orbital position at 28.5°E [17]. This is not surprising because indirect methods are known to suffer from unstable convergence for complex problems [8]. Thus, the hybrid method is an appealing choice for studies that simultaneously evaluate complex combinations of orbital perturbations, trajectory constraints, and optimization objectives.

The large difference in propellant expenditure between the optimal $J_2$-perturbed longitude-targeting solutions and the unperturbed free-longitude trajectories (Fig. 6) indicates a lack of robustness in the optimization algorithm. Albeit ideal for the demonstration purpose of this study, the implemented DE algorithm is the simplest DE variant and its stopping criteria appear to lead to premature convergence, which impairs the performance for simultaneous complex optimization objectives. This is indicated by the irregular curve of the Pareto front and the dispersion of the sub-optimal results in Fig. 6, which may be further deteriorated by unideal tuning of the DE parameters. It is thus recommended to employ a more sophisticated variant of the DE algorithm, with advanced stopping criteria for an enhanced convergence performance and lower computational times. An example of this is the DE algorithm available in ESA's Parallel Global Multiobjective Optimizer (PaGMO), which is additionally self-adaptive and avoids the fine-tuning effort. The authors acknowledge that the computational times presented in this demonstration are slower than current state of the art [18] software yet believe that upgrading the hardware, the optimization algorithm and optimizing the source code will yield a considerable margin for improvement in future research.

The thrust switching function hereby implemented constitutes a significant advancement with respect to the former hybrid optimization methods [11,12], which assumed constant thrust. The results show that this mechanism can successfully model non-thrusting arcs throughout the trajectory, thus allowing for accurate minimum-propellant optimization. This mechanism is very efficient because it requires only two additional optimization variables to model the engine on-off switching, while reaching the accuracy of analytical global optima.

The implemented OA propagation scheme is deemed to be a great asset for optimization of non-rendezvous transfers because it yielded a significant enhancement in the computational speed without jeopardizing the accuracy. Additionally, there is yet room for improvement, as indicated by the 0.96 kg OA-CI discrepancy (see Table 4) in the propellant expenditure, which varies linearly in time and should thus exhibit no averaging error. The use of the RK4 scheme was an ideal choice for the demonstration in this study due to its simplicity; however, it should be upgraded to a variable-step propagator in future research to reduce the propagation time.

The scaling procedure within the objective function proved to be effective in lessening the required user fine-tuning, allowing the weights of the final orbit error to be set to unity. Additionally, the user-specified allowed error successfully ensure that the optimizer does not invest unnecessary resources in further refining the solution beyond the tolerances,

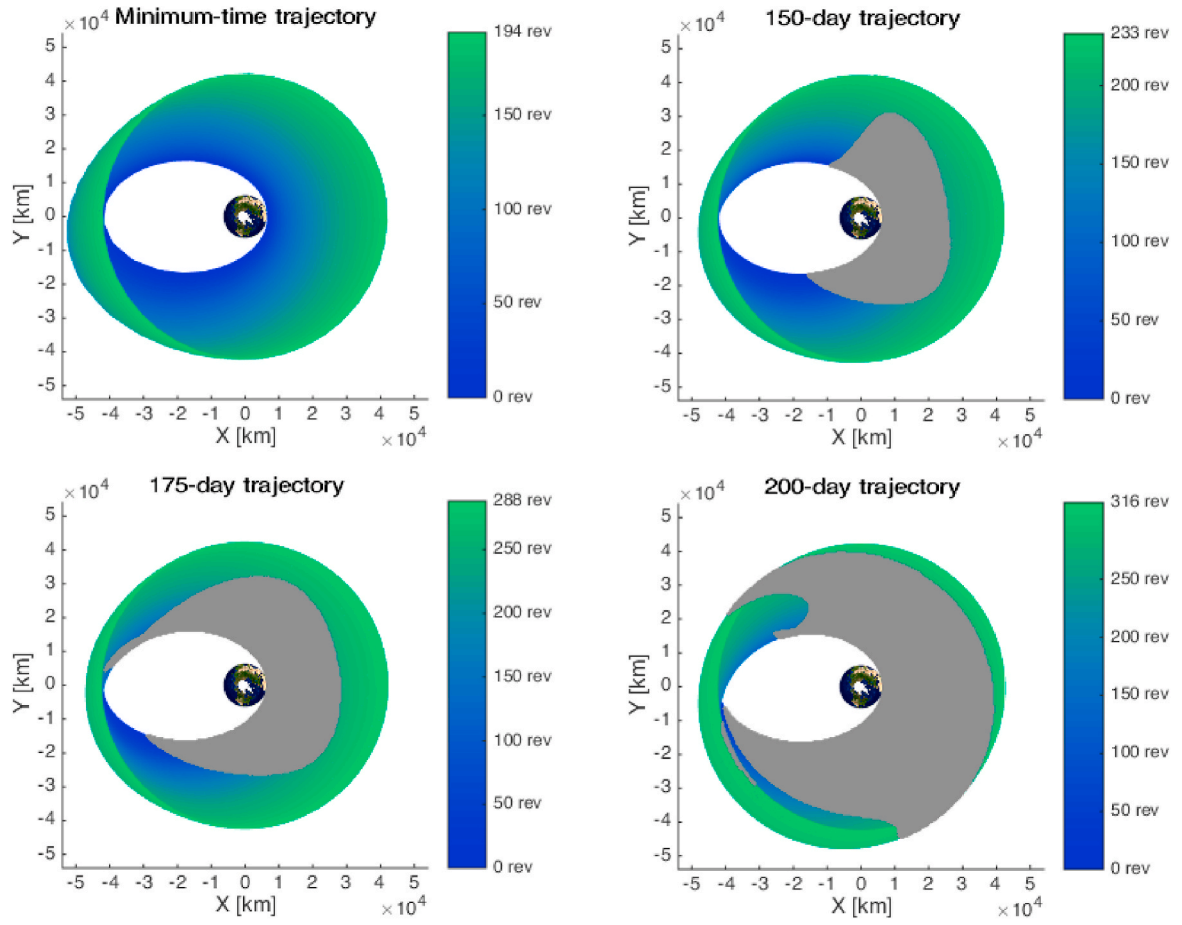


**Figs. 7.** 2D equatorial projections of the computed optimal minimum-propellant GTO(7°)-GEO(28.5°E) $J_2$-perturbed trajectory and coasting arcs (depicted in grey) for transfer times of 137 (minimum-time), 150, 175, and 200 days.

while enabling both a faster generation of near-optimal trajectories as well as high-accuracy solutions at longer computational times.

Lastly, it is worth drawing the attention to the practical suitability of the resulting optimizer. For example, the output thrust profile, an example of which is shown in Fig. 8 for the computed time-optimal trajectories, can be easily calculated from the propagation using the optimized parameters and can be directly harnessed for further operations, e.g. attitude control or power generation analyses. Furthermore, since the methodology is versatile for application in different problems, the hybrid optimizer can be easily integrated with other mission analysis tools to expand the simulation capabilities. For example, this could be harnessed to define further operational constraints during the propagation, e.g. maximum slew rates or attitude restrictions, or to allow for a configurable dynamical model, e.g. incorporate further orbital perturbations or eclipses. Similarly, the objective function can be easily tailored to optimize further variables computed with other utilities, such as the radiation fluence experienced throughout the transfer, the collision probability with other objects, or an indicator of the ground stations' visibility during orbit-raising. For these purposes, the presented hybrid method constitutes a great asset, superior to indirect approaches because it enables modifying to the dynamical model, constraints, or optimization objectives without the need to re-derive the optimal control laws.

## 6. Conclusions

This paper presents an accurate and flexible hybrid optimization method for low-thrust many-revolution trajectories, combining the benefits of both direct and indirect approaches while avoiding their drawbacks. Compared to former hybrid approaches, this methodology bridges the last shortcomings of former hybrid approaches for propellant-minimization, through a mechanism that allows for coasting (non-thrusting) arcs throughout the transfer. Additionally, an orbital averaging propagation scheme is implemented besides the classical continuous integration; with the former alternative allowing for a significant acceleration of the optimization process without jeopardizing its accuracy for non-rendezvous applications, whereas the latter retains the ability to target the final geodetic longitude. Furthermore, the objective function of the optimization is combined with a customizable error tolerance that provides the flexibility to perform accurate optimization as well as a faster generation of near-optimal trajectories. Despite the linearized EOM for the system co-states, the results for both an unperturbed and a $J_2$-perturbed GTO-GEO transfer exhibit a 0.03% error compared to the optimal solution of the reference indirect approach, and the minimum-propellant results yield a 0.4% error.

The resulting approach is demonstrated to be superior to direct methodologies because its analytical nature significantly reduces the design space and thus allows for practical computational times (30 min with orbital averaging and 118 min with continuous integration). Additionally, its computational nature makes it superior to purely indirect methods because 1) it provides an enhanced convergence radius, as shown by the simultaneous propellant-minimization and longitude-targeting of the GTO-GEO transfer, and 2) its optimal control laws are unaffected by modifications to the dynamical model, as shown by the inclusion of the $J_2$ acceleration. Nonetheless, more orbital perturbations must be incorporated – e.g. eclipses, third body forces, solar radiation pressure, and atmospheric drag – and more transfer cases must be evaluated in order to fully validate the hybrid method.

It should be emphasized that the goal of this paper is to demonstrate

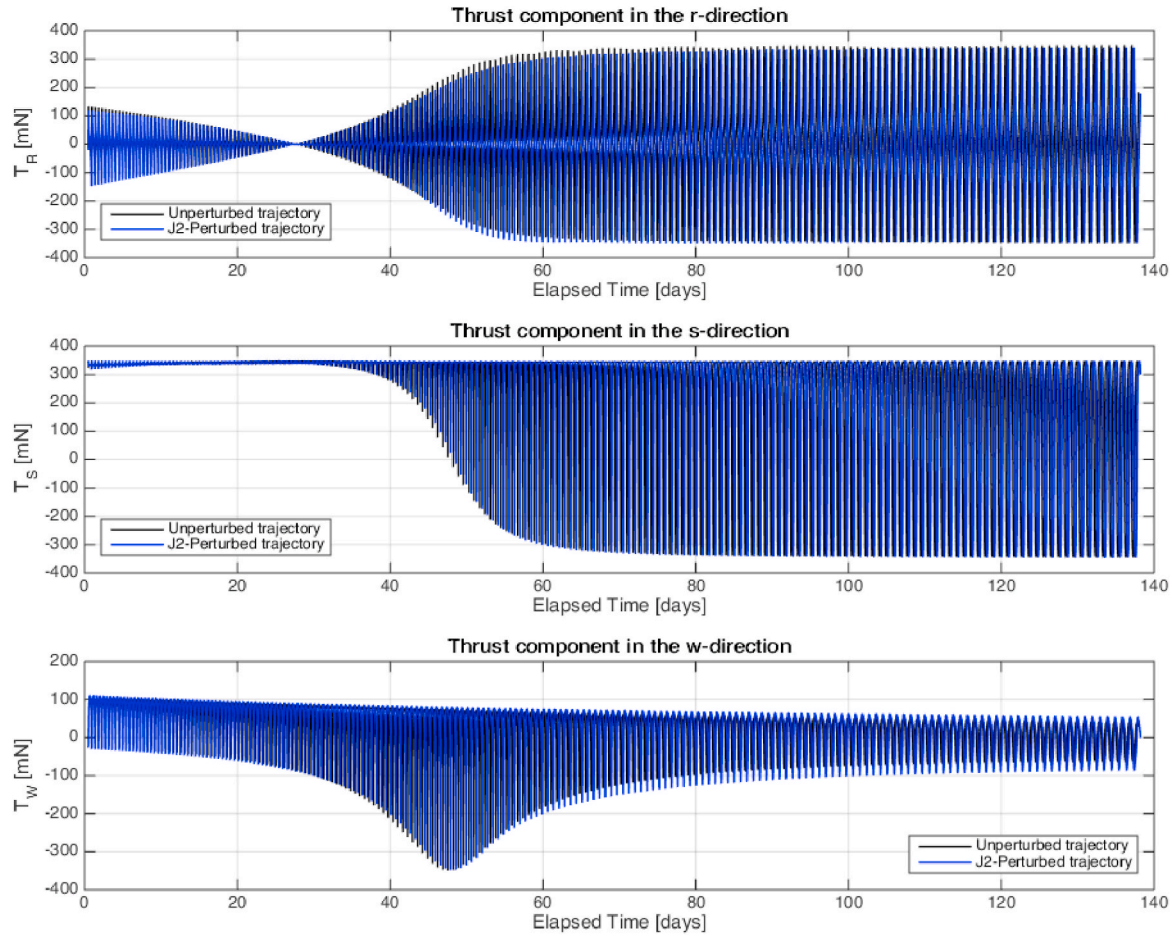


**Fig. 8.** Computed optimal thrust profiles of the unperturbed and $J_2$-perturbed GTO(7°)-GEO minimum-time trajectories in the r-direction, s-direction, and w-direction of the RSW frame.

the potential benefits of the hybrid approach rather than creating an operational tool. For the latter, there remains room for improvement in several areas, namely the need for a more sophisticated DE evolution, a variable-step integrator, hardware upgrades and optimization of the source code, all of which will provide a considerable margin in the required computational time. The upgrade of the optimization algorithm is deemed the next priority, because although the basic DE algorithm hereby employed was appropriate for this demonstration, its performance lacks the robustness that is necessary for an operational tool.

The implications of this research constitute a major advancement for terrestrial space missions design and satellite operations. The method is demonstrated to be a great resource for a wide range of applications, e.g. mission concept design, because: 1) its simplified co-state EOM enable its usage by users without profound experience in this field, and 2) its flexible formulation is applicable to a wide range of different problems without the need to analytically re-derive the optimal control problem. Furthermore, its enhanced convergence radius has the potential to allow for incorporating full perturbation models, complex combinations of operational constraints, and simultaneous optimization objectives. This can be a resourceful asset for example in small satellite missions using solar sailing or electric propulsion, because the accurate modelling of orbital perturbations is of paramount importance; as well as orbit-raising, station-keeping, and de-orbiting of full-electric scientific or telecom platforms, where the complex satellite systems may impose important trajectory constraints.

## Declaration of Competing Interest

None.

## Acknowledgements

This research is the outcome of a MSc thesis cooperation[1] between GMV Aerospace and Defence, Spain, and Delft University of Technology, The Netherlands. The author would like to thank the GMV department of Flight Dynamics and Operations for their continuous support and Antonio Lozano-Lima for making this fruitful cooperation possible. The access to GMV's Flight Dynamics solution ***focussuite*** enabled a thorough validation of the dynamical models and trajectory simulations. Furthermore, the access to GMV's in-house implementation of the reference indirect method [5] – and the re-derived formulations for the $J_2$ perturbation and longitude-targeting [17] – enabled the validation of some of the optimization results hereby presented, because the reference publication [5] did not cover these cases.

[1] The corresponding MSc thesis report is not yet published at the time of writing of this article. To request a copy, readers are encouraged to contact the corresponding author.

## Appendix A. Equations of Motion

The modified equinoctial elements are defined as follows [13,14]:

$$p = a(1 - e^2) \tag{A.1}$$

$$f = e\cos(\omega+\Omega) \tag{A.2}$$

$$g = e\sin(\omega+\Omega) \tag{A.3}$$

$$h = \tan\left(\frac{i}{2}\right)\cos\Omega \tag{A.4}$$

$$k = \tan\left(\frac{i}{2}\right)\sin\Omega \tag{A.5}$$

$$L = \Omega + \omega + \theta, \tag{A.6}$$

which can be converted to Keplerian coordinates:

$$a = \frac{p}{(1 - f^2 - g^2)} \tag{A.7}$$

$$e = \sqrt{f^2 + g^2} \tag{A.8}$$

$$i = 2\text{atan}(\sqrt{h^2 + k^2}) \tag{A.9}$$

$$\Omega = \text{atan2}\left(\frac{k}{\sqrt{h^2 + k^2}}, \frac{h}{\sqrt{h^2 + k^2}}\right) \tag{A.10}$$

$$\omega = \text{atan2}(gh - fk, fh + gk) \tag{A.11}$$

$$\theta = L - \Omega - \omega \tag{A.12}$$

The dynamics matrix $\boldsymbol{A}(\vec{x})$ and the vector $\vec{b}$ describing the Gauss' form of the Lagrange planetary equations are defined in Eqs. A.13-A.14:

$$\boldsymbol{A}(\vec{x}) = \begin{bmatrix} 0 & \sqrt{\frac{p}{\mu}}\frac{2p}{w_1} & 0 \\ \sqrt{\frac{p}{\mu}}\sin L & \sqrt{\frac{p}{\mu}}\frac{1}{w_1}[(w_1+1)\cos L + f] & \sqrt{\frac{p}{\mu}}\frac{g}{w_1}[h\sin L - k\cos L] \\ & -\sqrt{\frac{p}{\mu}}\cos L & \sqrt{\frac{p}{\mu}}\frac{1}{w_1}[(w_1+1)\sin L + g] \\ & & \sqrt{\frac{p}{\mu}}\frac{f}{w_1}[h\sin L - k\cos L] \\ 0 & 0 & \sqrt{\frac{p}{\mu}}\frac{w_2\cos L}{2w_1} \\ 0 & 0 & \sqrt{\frac{p}{\mu}}\frac{w_2\sin L}{2w_1} \\ 0 & 0 & \sqrt{\frac{p}{\mu}}\frac{1}{w_1}[h\sin L - k\cos L] \end{bmatrix} \tag{A.13}$$

$$\vec{b} = \left[0 0 0 0 0 \sqrt{\mu p}\left(\frac{w_1}{p}\right)^2, -\frac{T}{g_0 I_{sp}}\right]^T \tag{A.14}$$

where $g_0 = 9.80665\ \text{ms}^{-1}$ is the gravitational acceleration of Earth at sea level, and $w_1$ and $w_2$ are auxiliary variables:

$$w_1 = 1 + f\cos L + g\sin L \tag{A.15}$$

$$w_2 = 1 + h^2 + k^2 \tag{A.16}$$

The RSW $J_2$ acceleration vector is given by Ref. [19]:

$$a_{J_2,r} = -\frac{3\mu J_2 R_E^2}{2r^4}\left(1 - 12\frac{\kappa_1^2}{\kappa_3}\right) \tag{A.17}$$

$$a_{J_2,\gamma} = -\frac{12\mu J_2 R_E^2}{r^4}\left(\frac{\kappa_1\kappa_2}{\kappa_3}\right) \tag{A.18}$$

$$a_{J_2,h} = -\frac{6\mu J_2 R_E^2}{r^4}\left(\frac{\kappa_1(1 - h^2 - k^2)}{\kappa_3}\right), \tag{A.19}$$

where $\mu = 3.9860044 \times 10^5\ \text{km}^3\text{s}^{-2}$ is the Earth gravitational parameter, $R_E = 6378.136$ km is the equatorial radius of Earth and $J_2 = 1.082626 \times 10^{-3}$ is the second order Earth oblateness constant. Moreover, $\kappa_1$, $\kappa_2$, and $\kappa_3$ are auxiliary variables:

$$\kappa_1 = h\sin(L) - k\cos(L) \tag{A.20}$$

$$\kappa_2 = h\cos(L) + k\sin(L) \tag{A.21}$$

$$\kappa_3 = (1 + h^2 + k^2)^2 \tag{A.22}$$

## Appendix B. Optimal Control Law Derivation

The optimal control law follows from the necessary conditions in Eqs. (3.7) and (3.8). First, Eq. (3.7) is applied to Eq. (3.6) with respect to angle $\alpha$ to derive the optimal yaw steering control law $\alpha^*(t)$. After some manipulation, one obtains:

$$\tan\alpha = \frac{\Lambda^{\alpha}_{f,1} - \Lambda^{\alpha}_{g,1}}{\Lambda^{\alpha}_{p} + \Lambda^{\alpha}_{f,2} + \Lambda^{\alpha}_{g,2}}, \tag{B.1}$$

where the following auxiliary variables are used for simplicity:

$$\Lambda^{\alpha}_{p} = \lambda_p\sqrt{\frac{p}{\mu}}\frac{2p}{w_1}\cos\beta \tag{B.2}$$

$$\Lambda^{\alpha}_{f,1} = \lambda_f\sqrt{\frac{p}{\mu}}\cos\beta\sin L \tag{B.3}$$

$$\Lambda^{\alpha}_{g,1} = \lambda_g\sqrt{\frac{p}{\mu}}\cos\beta\cos L \tag{B.4}$$

$$\Lambda^{\alpha}_{f,2} = \lambda_f\sqrt{\frac{p}{\mu}}\frac{[(w_1+1)\cos L + f]\cos\beta}{w_1} \tag{B.5}$$

$$\Lambda^{\alpha}_{g,2} = \lambda_g\sqrt{\frac{p}{\mu}}\frac{[(w_1+1)\sin L + g]\cos\beta}{w_1}, \tag{B.6}$$

where the terms $\sqrt{p/\mu}$ and $\cos\beta$ may be removed for simplicity. The expressions for $\sin\alpha^*$ and $\cos\alpha^*$ can be derived from Eq. B.1 using trigonometric identities, and their correct sign for a minimum follow from Eq. (3.8):

$$\sin\alpha^* = \frac{-(\Lambda^{\alpha}_{f,1} - \Lambda^{\alpha}_{g,1})}{\sqrt{(\Lambda^{\alpha}_{f,1} - \Lambda^{\alpha}_{g,1})^2 + (\Lambda^{\alpha}_{p} + \Lambda^{\alpha}_{f,2} + \Lambda^{\alpha}_{g,2})^2}} \tag{B.7}$$

$$\cos\alpha^* = \frac{-(\Lambda^{\alpha}_{p} + \Lambda^{\alpha}_{f,2} + \Lambda^{\alpha}_{g,2})}{\sqrt{(\Lambda^{\alpha}_{f,1} - \Lambda^{\alpha}_{g,1})^2 + (\Lambda^{\alpha}_{p} + \Lambda^{\alpha}_{f,2} + \Lambda^{\alpha}_{g,2})^2}} \tag{B.8}$$

Similarly, the necessary condition in Eq. (3.7) can be applied to Eq. (3.6) with respect to the control angle $\beta$ to obtain the optimal pitch steering control law $\beta^*(t)$:

$$\tan\beta^* = \frac{-\Lambda^{\beta}_{f,3} + \Lambda^{\beta}_{g,3} + \Lambda^{\beta}_{h} + \Lambda^{\beta}_{k}}{\Lambda^{\beta}_{p} + \Lambda^{\beta}_{f,1} + \Lambda^{\beta}_{f,2} - \Lambda^{\beta}_{g,1} + \Lambda^{\beta}_{g,2}}, \tag{B.9}$$

which employs the following auxiliary variables:

$$\Lambda^{\beta}_{p} = \lambda_p\sqrt{\frac{p}{\mu}}\frac{2p}{w_1}\cos\alpha^* \tag{B.10}$$

$$\Lambda^{\beta}_{f,1} = \lambda_f\sqrt{\frac{p}{\mu}}\sin L\sin\alpha^* \tag{B.11}$$

$$\Lambda^{\beta}_{g,1} = \lambda_g\sqrt{\frac{p}{\mu}}\cos L\sin\alpha^* \tag{B.12}$$

$$\Lambda^{\beta}_{f,2} = \lambda_f\sqrt{\frac{p}{\mu}}\frac{1}{w_1}[(w_1+1)\cos L + f]\cos\alpha^* \tag{B.13}$$

$$\Lambda^{\beta}_{g,2} = \lambda_g\sqrt{\frac{p}{\mu}}\frac{1}{w_1}[(w_1+1)\sin L + g]\cos\alpha^* \tag{B.14}$$

$$\Lambda^{\beta}_{f,3} = \lambda_f\sqrt{\frac{p}{\mu}}\frac{g}{w_1}(h\sin L - k\cos L) \tag{B.15}$$

$$\Lambda^{\beta}_{g,3} = \lambda_g\sqrt{\frac{p}{\mu}}\frac{f}{w_1}(h\sin L - k\cos L) \tag{B.16}$$

$$\Lambda^{\beta}_{h} = \lambda_h\sqrt{\frac{p}{\mu}}\frac{w_2\cos L}{2w_1} \tag{B.17}$$

$$\Lambda_k^\beta = \lambda_k \sqrt{\frac{p}{\mu}} \frac{w_2 \sin L}{2w_1} \tag{B.18}$$

Again, the expressions for $\sin\beta^*$ and $\cos\beta^*$ can be derived from Eq. B.9 using trigonometric identities, followed by substituting the previous equations for $\sin\alpha^*$ and $\cos\alpha^*$ and applying the minimum condition in Eq. (3.8):

$$\sin\beta^* = \frac{-(-\Lambda_{f,3}^\beta + \Lambda_{g,3}^\beta + \Lambda_h^\beta + \Lambda_k^\beta)}{\sqrt{(-\Lambda_{f,3}^\beta + \Lambda_{g,3}^\beta + \Lambda_h^\beta + \Lambda_k^\beta)^2 + (\Lambda_p^\beta + \Lambda_{f,1}^\beta - \Lambda_{g,1}^\beta + \Lambda_{f,2}^\beta + \Lambda_{g,2}^\beta)^2}} \tag{B.19}$$

$$\cos\beta^* = \frac{-(\Lambda_p^\beta + \Lambda_{f,1}^\beta - \Lambda_{g,1}^\beta + \Lambda_{f,2}^\beta + \Lambda_{g,2}^\beta)}{\sqrt{(-\Lambda_{f,3}^\beta + \Lambda_{g,3}^\beta + \Lambda_h^\beta + \Lambda_k^\beta)^2 + (\Lambda_p^\beta + \Lambda_{f,1}^\beta - \Lambda_{g,1}^\beta + \Lambda_{f,2}^\beta + \Lambda_{g,2}^\beta)^2}} \tag{B.20}$$

The previous control laws in Eqs. B.7-B.8, and B.19-B.20 can be substituted without further simplification in Eqs. A.13-A.14, which feature only sine and cosine terms.

Lastly, the necessary condition in Eq. (3.7) is applied to Eq. (3.6) with respect to the thrust magnitude $T$:

$$\frac{\partial \mathscr{H}_3}{\partial T} = \Lambda_p^\beta \cos\beta^* \frac{1}{m} + \Lambda_h^\beta \sin\beta^* \frac{1}{m} + \Lambda_k^\beta \sin\beta^* \frac{1}{m} + [\Lambda_{f,1}^\beta \cos\beta^* + \Lambda_{f,2}^\beta \cos\beta^* - \Lambda_{f,3}^\beta \sin\beta^*] \frac{1}{m} \tag{B.21}$$

$$+ [-\Lambda_{g,1}^\beta \cos\beta^* + \Lambda_{g,2}^\beta \cos\beta^* + \Lambda_{g,3}^\beta \sin\beta^*] \frac{1}{m} - \lambda_m \frac{1}{g_0 I_{sp}}$$

This time, however, the condition yields a bang-bang problem instead of a single expression for the optimal thrust magnitude because the Hamiltonian varies linearly with control parameter $T$ [7]:

$$T(t) = T_{max} \quad \text{if } S_t(t) < 0 \tag{B.22}$$

$$T(t) = 0 \quad \text{if } S_t(t) > 0, \tag{B.23}$$

where the switching function $S_t$ is defined as $S_t = \partial\mathscr{H}_3/\partial T$. It should be clarified that a third condition may exist, Eq. B.27, yielding a singular control problem:

$$0 < T < T_{max} \text{ if } S_t = 0 \text{ and } \frac{dS_t}{dt} = 0 \tag{B.24}$$

However, the necessary conditions for such singular arc are deemed unfeasible due to the numeric nature of the methodology and this potential third condition is neglected.

## Appendix C

*Nomenclature*

| | |
|---|---|
| $\vec{\text{æ}}$ | trajectory terminal boundary conditions vector |
| $a$ | semi-major axis |
| $\vec{a}_T$ | thrust acceleration vector |
| $\vec{a}_{J_2}$ | acceleration vector caused by the $J_2$ perturbation |
| $\boldsymbol{A}$ | dynamics matrix of the trajectory state dynamics |
| $\vec{b}$ | offset vector of the trajectory state dynamics |
| $e$ | eccentricity |
| $e_j$ | final orbit error of the $j^{\text{th}}$ element in $\vec{\text{æ}}$ |
| $f$ | second equinoctial element |
| $g$ | third equinoctial element |
| $h$ | fourth equinoctial element |
| $\mathscr{H}$ | Hamiltonian equation |
| $i$ | inclination |
| $I_{sp}$ | specific impulse |
| $k$ | fifth equinoctial element |
| $L$ | true longitude |
| $\mathscr{L}$ | Lagrange term in the optimization cost function |
| $m$ | spacecraft total mass |
| $m_p$ | required propellant mass |
| $n_{oa}$ | number of orbital averaging propagation arcs |
| $n_p$ | number of propagation steps per orbital revolution |
| $p$ | semi-latus rectum |
| $P$ | instantaneous orbital period of the trajectory |
| $\hat{q}$ | unit vector of the $\boldsymbol{Q}$ frame |
| $\boldsymbol{Q}_{RSW}$ | matrix defining the RSW frame |
| $\vec{\alpha}$ | trajectory initial boundary conditions vector |
| $\vec{r}$ | satellite position vector |
| $t$ | time |

| | |
|---|---|
| $T$ | magnitude of the thrust vector |
| $\vec{u}$ | control variables vector |
| $\vec{v}$ | satellite velocity vector |
| $\vec{x}$ | propagated trajectory state vector |
| $W_t$ | cost function weight for the time-of-flight |
| $W_m$ | cost function weight for the mass expenditure |
| $W_j$ | cost function weight for the $j^{\text{th}}$ element in $\vec{\text{æ}}$ |
| $\alpha$ | yaw steering angle |
| $\beta$ | pitch steering angle |
| $\theta$ | true anomaly |
| $\vec{\lambda}$ | system co-state, or adjoint, vector |
| $\Lambda$ | –geodetic longitude |
| $\varepsilon_j$ | scaled final orbit error of the $j^{\text{th}}$ element in $\vec{\text{æ}}$ |
| $\Phi$ | Mayer term in the optimization cost function |
| $\omega$ | argument of perigee |
| $\Omega$ | right ascension of the ascending node |
| $*$ | optimal value(s) of a variable or vector |
| $^{\text{T}}$ | transpose of a vector |
| $_0$ | initial value at the start of the propagation |
| $_{avg}$ | averaged value(s) of a variable or vector |
| $_{\text{d}}$ | total disturbance |
| $_f$ | final value at the end of the propagation |
| $_j$ | placeholder for the $j = 1,2, \ldots, 6$elements in vectors $\vec{\lambda}$ and $\vec{\text{æ}}$ |
| $_{LB}$ | lower bound(s) of a variable or vector |
| $_{UB}$ | upper bound(s) of a variable or vector |
| $_r$ | direction of the Earth-satellite vector |
| $_s$ | direction normal to the Earth-satellite vector |
| $_w$ | direction of the angular momentum vector |

## References


[1] J. Gil-Fernandez, M.A. Gomez-Tierno, Practical method for optimization of low-thrust transfers, J. Guid. Contr. Dynam. 33 (2010) 1927–1931.
[2] D.J. Gondelach, R. Noomen, Hodographic-shaping method for low-thrust interplanetary trajectory design, J. Spacecraft Rockets 52 (2015) 728–738.
[3] J.T. Betts, Optimal low-thrust orbit transfers with eclipsing, Optim. Contr. Appl. Methods 36 (2015) 218–240.
[4] E. Taheri, O. Abdelkhalik, Initial three-dimensional low-thrust trajectory design, Adv. Space Res. 57 (2016) 889–903.
[5] J.M. Sanchez, A. Campa, Automation of multi-revolution low-thrust transfer optimization via differential evolution, American Astronautical Society 14 (2014) 1–20.
[6] S. Geffroy, R. Epenoy, Optimal low-thrust transfers with constraints – generalization of averaging techniques, Acta Astronaut. 41 (1997) 133–149.
[7] L.S. Pontryagin, Mathematical Theory of Optimal Processes, CRC Press, 1986.
[8] J.T. Betts, Survey of numerical methods for trajectory optimization, J. Guid. Contr. Dynam. 21 (1998) 193–207.
[9] P. Wei, L. Changhou, Direct optimization of low-thrust transfers using averaging techniques based on fourier series expansion, 4th Int. Joint Conference on Computational Sciences and Optimization, Barcelona. Spain, 2010, pp. 46–50.
[10] D. Jimenez-Lluva, B. Root, M. Gómez-Jenkins, Hybrid optimization of low-thrust many-revolution orbital transfers, The 4S Symposium, Sorrento, Italy, 28 May – 1 June 2018.
[11] C.A. Kluever, Low-thrust trajectory optimization using orbital averaging and control parameterization, in: B.A. Conway (Ed.), Spacecraft Trajectory Optimization, Cambridge University Press, New York, 2010, pp. 112–138.
[12] M. Gomez-Jenkins, Development of a Low-Thrust Multi-Objective Trajectory Optimization Tool for CleanSpace One. IAC-15-E2.1.8, 66th International Astronautical Cong, Ress, Jerusalem, Israel, 2015, pp. 12–16 October.
[13] M.J.H. Walker, B. Ireland, J. Owens, A set of modified equinoctial orbit elements, Celestial Mech. 36 (1985) 409–419.
[14] M.J.H. Walker, Erratum – a set of modified equinoctial orbit elements, Celestial Mech. 38 (1986) 391–392.
[15] R. Storn, K. Price, Differential evolution a simple and efficient heuristic for global optimization over continuous spaces, J. Global Optim. 11 (1997) 341–359.
[16] F.S. Wang, Differential Evolution Implementation in Fortran 90, National Chung Cheng University, 2010, https://www1.icsi.berkeley.edu/~storn/DE_FORTRAN90.f90 , Accessed date: 23 February 2019.
[17] P.J. Montealegre-Avila, Algorithm Analysis for Operational Implementation of GEO Transfer Orbits Using Electric Propulsion, Master of science thesis, Universidad Politecnica de Madrid, 2015.
[18] A.E. Petropoulos, Z.B. Tarzi, G. Lantoine, T. Dargent, R. Epenoy, Techniques for designing many-revolution, electric-propulsion trajectories, Adv. Astronaut. Sci. 152 (3) (2014) 2367–2385.
[19] J.A. Kechichian, Minimum-time constant acceleration orbit transfer with first-order oblateness effect, J. Guid. Contr. Dynam. 23 (2000) 595–603.


Ir. David Jimenez-Lluva is an alumnus of the faculty of Aerospace Engineering at the Delft University of Technology. His Master of Science thesis research focused on the optimization of many-revolution low-thrust trajectories and was awarded the second student prize of the graduate competition at the 69th International Astronautical Congress (Bremen, 2018). This paper constitutes the summary of this research and reveals the methodology that he developed. He is currently employed by GMV as a flight dynamics engineer at the CNES space centre in Toulouse, France.

Dr. ir. Bart Root is a lecturer and researcher at the Department of Space Engineering, faculty of Aerospace Engineering at the Delft University of Technology. His teachings are centred around Satellite Operations and Tracking and Earth Observation. His research focusses on satellite gravity constraints in modelling the solid Earth-like processes, such as lithosphere structure, mantle convection and seismology constraints. Bart Root has developed an on-campus satellite tracking station, which is able to track and receive satellite radio signals and is used by students in their curriculum. Bart Root was awarded the Innovative Teaching Talent 2017 award.